JOURNAL OF GEOPHYSICAL RESEARCH, VOL. 103, NO. D24, PAGES 31,943–31,953, DECEMBER 27, 1998

Airborne spectral measurements of surface anisotropy during SCAR–B

Si-Chee Tsay and Michael D. King
NASA Goddard Space Flight Center, Greenbelt, Maryland.

G. Thomas Arnold and Jason Y. Li
Space Applications Corporation, Vienna, Virginia.

Abstract. During the Smoke, Clouds, and Radiation–Brazil (SCAR–B) deployment, angular distributions of spectral reflectance for vegetated surfaces and smoke layers were measured using the scanning cloud absorption radiometer (CAR) mounted on the University of Washington C-131A research aircraft. The CAR contains 13 narrowband spectral channels between 0.3 and 2.3 μm with a 190° scan aperture (5° before zenith to 5° past nadir) and 1° instantaneous field of view. The bidirectional reflectance is obtained by flying a clockwise circular orbit above the surface, resulting in a ground track ~3 km in diameter within about 2 min. Although the CAR measurements are contaminated by minor atmospheric effects, results show distinct spectral characteristics for various types of surfaces. Spectral bidirectional reflectances of three simple and well-defined surfaces are presented: cerrado (August 18, 1995) and dense forest (August 25, 1995), both measured in Brazil under nearly clear-sky conditions, and thick smoke layers over dense forest (September 6 and 11, 1995). The bidirectional reflectances of cerrado and dense forest revealed fairly symmetric patterns along the principal plane, with varying maximal strengths and widths spectrally in the backscattering direction. In the shortwave-infrared region the aerosol effect is very small due to low spectral optical depth. Also, these backscattering maxima can be seen on the bidirectional reflectance of smoke layer over dense forest. These detailed measurements of the angular distribution of spectral reflectance can be parameterized by a few independent variables and utilized to retrieve either surface characteristics or aerosol microphysical and optical properties (e.g., size distribution and single-scattering parameters), if proper physical and radiation models are used. The spectral-hemispherical albedo of these surfaces is obtained directly by integrating all angular measurements and is compared with the measured nadir reflectance. Using CAR nadir reflectance as a surrogate for spectral-hemispherical albedo can cause albedos to be underestimated by 10–60%, depending on solar zenith angle.

1. Introduction

Surface spectral bidirectional reflectance is a major parameter of interest to the biospheric sciences, remote sensing, and global change communities. For example, the pronounced reflectance peak at the backscattering range of vegetated surfaces, known as the "hot spot" or "opposition surge" [cf. *Suits*, 1972; *Hapke*, 1993], is found to be closely related to the state of several biophysical and physical parameters [e.g., *Pinty and Verstraete*, 1991; *Strahler and Jupp*, 1990]. The surface bidirectional reflectance also plays a crucial role in the radiative energy balance, since it is required to determine (1) the spectral and spectrally integrated albedo [e.g., *Kriebel*, 1979; *Ranson et al.*, 1991] and (2) the top-of-the-atmosphere angular distribution of the radiance field [e.g., *Hapke*, 1993]. It is common practice to assume a Lambertian (isotropic) surface in general circulation models or global climate models (GCMs) and/or to estimate albedo from satellite/aircraft measurements close to nadir [*Barnsley et al.*, 1994, and references therein]. The Lambertian assumption is invalid for most natural surfaces, and estimations of albedo from nadir measurements have been shown to be in error by as much as 45% [e.g., *Kimes and Sellers*, 1985; *Kimes et al.*, 1987]. In turn, a vital piece of information for climate studies and remote sensing applications is the anisotropy of the surface reflectance.

For the past three decades the spectral anisotropy of a variety of natural surfaces has been observed using various types of ground-based instruments [e.g., *Perovich*, 1994; *Deering et al.*, 1992, and references therein] and airborne instruments [e.g., *Salomonson and Marlatt*, 1968; *Kriebel*, 1978; *Barnsley*, 1984; *King*, 1992; *Ranson et al.*, 1994]. Opportunities for such measurements from spaceborne sensors will soon exist through many national and international collaborations of Earth Observing Systems [cf. *Asrar and Greenstone*, 1995]. Offering larger space and timescales, satellite measurements will play a major role in providing a more complete and necessary understanding of the Earth's dynamic ecosystems and atmosphere and the processes that govern their changes. However, because of sensor geometry and orbital characteristics of a particular satellite, measurements to describe the surface anisotropy may not be acquired adequately to meet the sampling requirements [*Barnsley et al.*, 1994]. Thus better understanding the characteristics of surface anisotropy requires coordinated ground-

Paper number 98JD01167.
0148-0227/98/98JD-01167$09.00

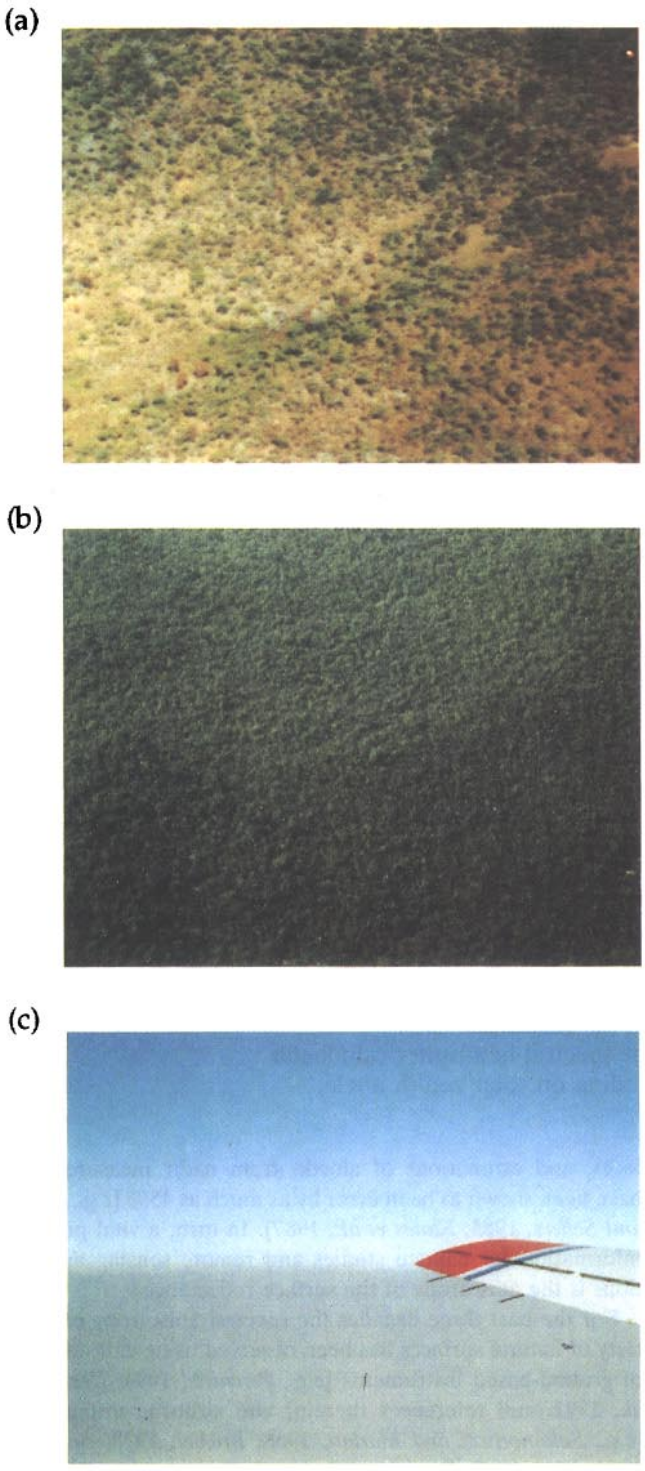

Plate 1. Photographs of (a) cerrado, (b) dense forest, and (c) smoke layer, taken during SCAR-B from the University of Washington C-131A aircraft.

based, airborne, and spaceborne measurements; some studies may even require long-term continuity. In an intensive field observation period, airborne measurements from multispectral, high-speed scanning radiometers provide the most mobile and efficient means of fulfilling these needs. One such opportunity to measure surface anisotropy was available during the Smoke, Clouds, and Radiation–Brazil (SCAR–B) field campaign [*Kaufman et al.*, this issue].

Instruments best designed for measuring surface bidirectional reflectance should meet the following two requirements: (1) provide multiple viewing angle measurements in a short period of time to minimize the effects of changing source and target conditions and (2) simultaneously measure the downwelling radiance from the source and upwelling radiance from the target. During SCAR–B, one such multispectral scanning radiometer flew aboard the University of Washington Convair C-131A aircraft and acquired data of spectral bidirectional reflectance over a large area in Brazil under various environmental conditions. As part of the SCAR–B mission, the scientific objectives were twofold: (1) to characterize surface spectral bidirectional reflectances, in terms of which their angular distributions can be described and parameterized with a few independent variables, and (2) to correlate clear-sky surface off-nadir reflectances between visible and shortwave-infrared wavelengths for use in remote sensing and retrievals of aerosols over land [*Kaufman et al.*, 1996]. In this paper we focus on documenting and discussing the measurements of three types of surface bidirectional reflectances and leave the parameterization and modeling work (e.g., atmospheric correction) to future contributions.

The following section defines the surface bidirectional reflectance distribution function (BRDF) and discusses some considerations in remote sensing and applications. The instrumentation and data collection strategy are laid out in section 3, followed by discussion of surface spectral anisotropy and albedo results in section 4. A brief summary of this study and future work is given in section 5.

2. Definitions and Considerations

According to the National Bureau of Standards the spectral bidirectional reflectance distribution function [*Nicodemus et al.*, 1977] ρ_λ is defined as

$$\rho_\lambda(\theta_r, \phi_r; \theta_i, \phi_i) = \frac{dI_\lambda(\theta_r, \phi_r; \theta_i, \phi_i)}{dF_\lambda(\theta_i, \phi_i)}, \qquad (1)$$

which is a ratio of two derivatives; F_λ is the collimated irradiance illuminating at zenith angle θ_i and azimuth angle ϕ_i; and I_λ is the corresponding reflected radiance at angles θ_r and ϕ_r. In (1), ρ_λ is in units of sr^{-1}. Theoretically, the principle of reciprocity, $\rho_\lambda(\theta_r, \phi_r; \theta_i; \phi_i) = \rho_\lambda(121_r, \phi_i; \theta_r, \phi_r)$, is well satisfied [e.g., *Hapke*, 1993]. However, in dealing with actual measurements and applications, there are many factors that need to be considered to appropriately describe the distribution of bidirectional reflectance.

Measurements from radiometric instrumentation are always confined within an instantaneous field of view (IFOV), a finite solid angle defining the incident and viewing directions, not a derivative. Added to this is that under natural conditions, photon scattering and/or absorption may occur before photons are received by the instrument sensors. In turn, additional amounts of diffuse radiation may be detected by the sensors. Thus (1) is not practical in defining measurements of surface anisotropy.

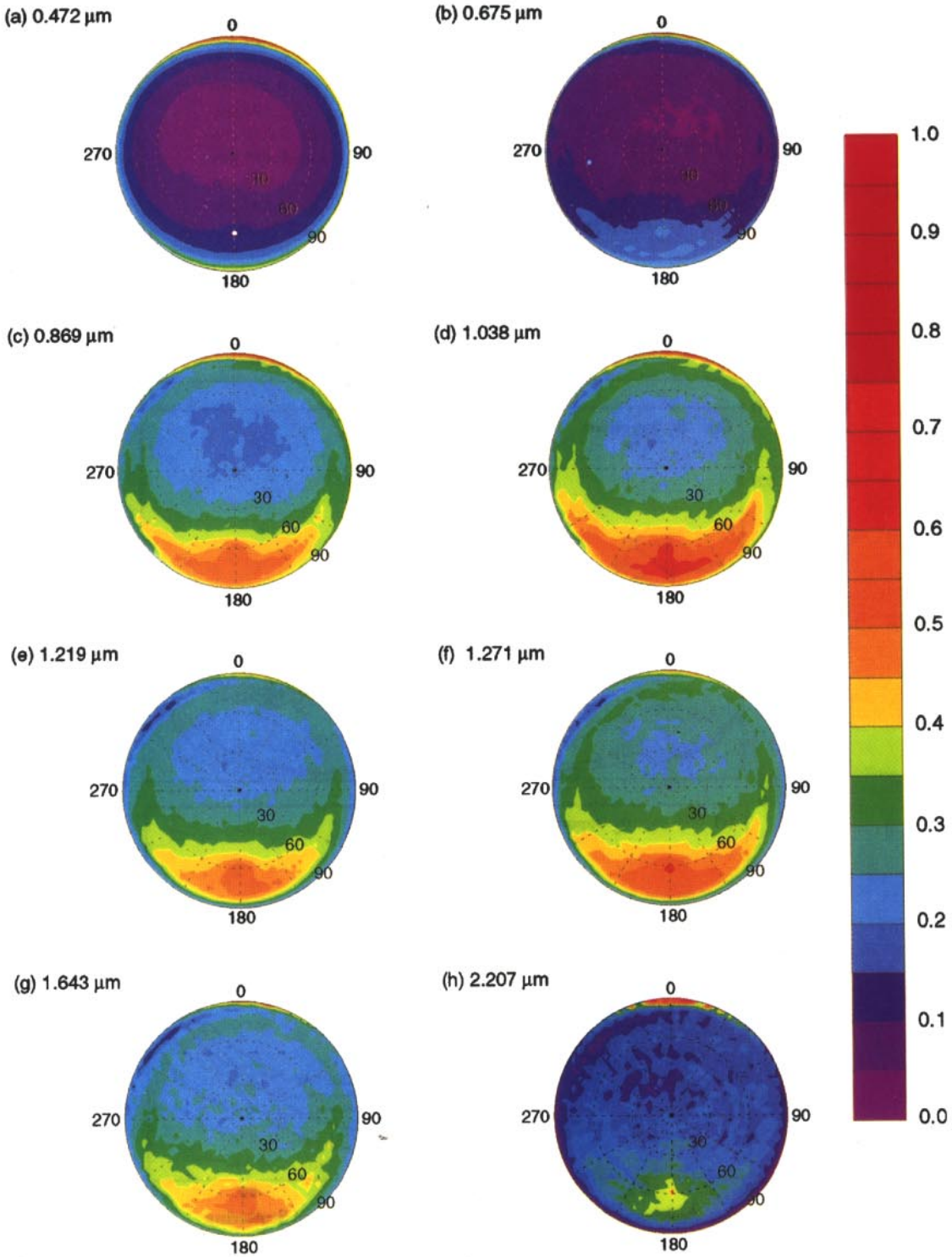

Plate 2. Spectral measurements of surface bidirectional reflectance over cerrado on August 18, 1995, during SCAR-B. The location of the antisolar point at $\theta = 60°$ and $\phi = 180°$ is indicated in Plate 2a.

In addition, depending on the properties of the intervening media (e.g., concentration and optical characteristics of molecules and particles along slant paths) and the state of the reflecting surface (e.g., leaf orientation, wetness), the bidirectional reflectance pairs measured at different times may not obey the principle of reciprocity. To characterize the surface anisotropy from spectral measurements, we adopt the definition, commonly used in the atmospheric radiation community [e.g., *van de Hulst*, 1980], of bidirectional reflection function (BRF, R_λ) given as

$$R_\lambda(\theta, \theta_0, \phi) = \frac{\pi I_\lambda(\theta, \theta_0, \phi)}{\mu_0 F_\lambda}, \tag{2}$$

where θ and θ_0 are, respectively, the viewing and illumination zenith angles; ϕ is the azimuth angle between the viewing and

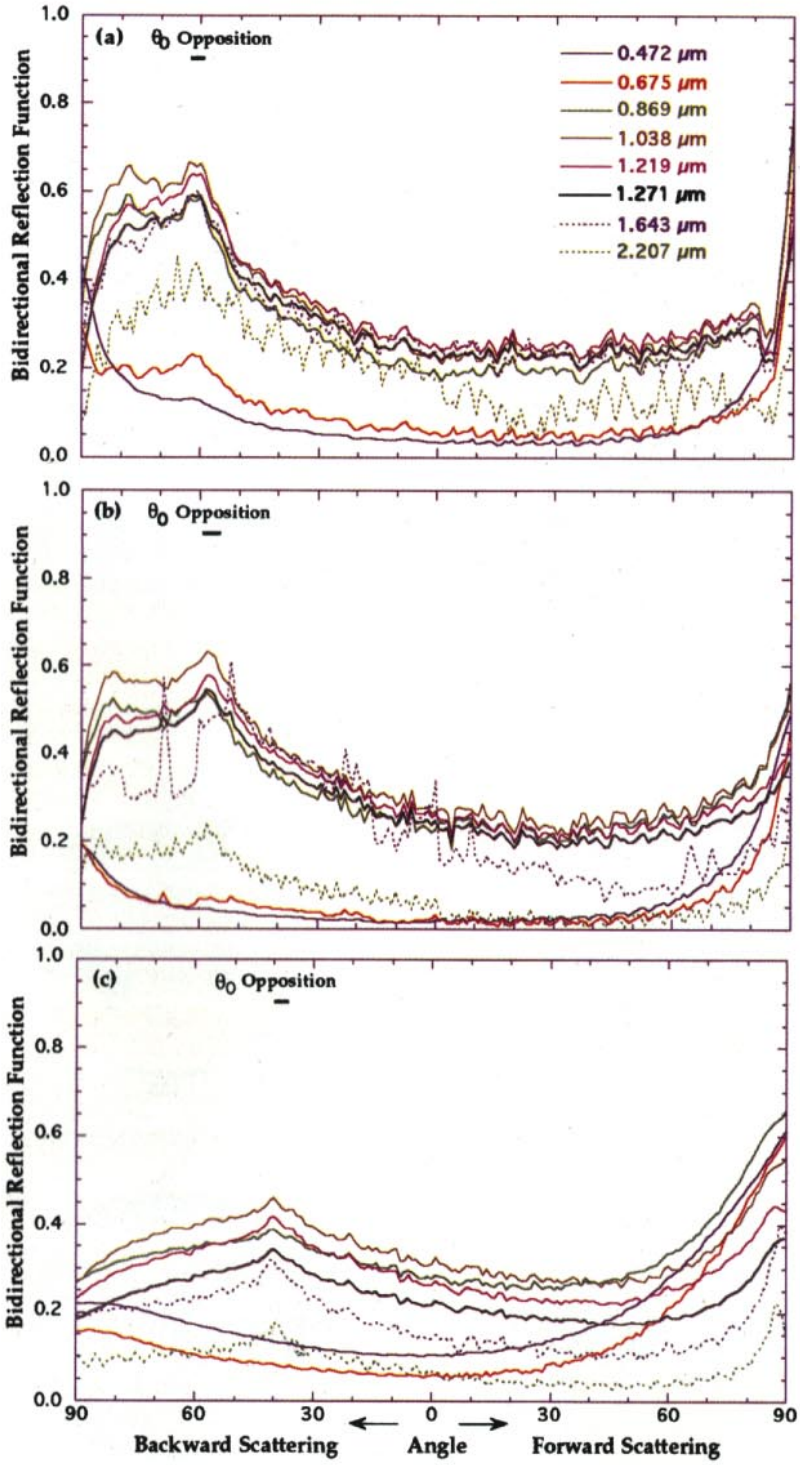

Plate 3. Angular distribution of bidirectional reflectance function (BRF) in the principal plane for (a) cerrado, (b) dense forest, and (c) smoke layer during SCAR-B.

illumination directions; and $\mu_0 = \cos\theta_0$. Thus the BRF in (2) is dimensionless and directly normalized to the reference illumination irradiance. This avoids the potential problems that the illumination source may not be covered entirely by the instrument IFOV and/or not be captured fully by the viewing geometry, as well as to prevent possible signal saturation due to instrument dynamical range. Similarly for the spectral albedo r_λ, radiances received by the detector from all viewing directions/solid angles are integrated (or summed up for all IFOVs). By substituting (2) it becomes

$$r_\lambda(\theta_0) = \frac{1}{\pi}\int_0^{2\pi}\int_0^{\pi/2} R_\lambda(\theta, \theta_0, \phi)\cos\theta\sin\theta\, d\theta\, d\phi, \tag{3}$$

$$\cong \frac{1}{\mu_0 F_\lambda}\left[\sum_{i=1}^{M}\sum_{j=1}^{N} I_\lambda(\theta_i, \theta_0, \phi_j)\cos\theta_i\sin\theta_i\,\Delta\theta_i\,\Delta\phi_j\right],$$

where (i, j) are, respectively, the indices of (θ, ϕ) for discretization (M, N terms) over the hemisphere.

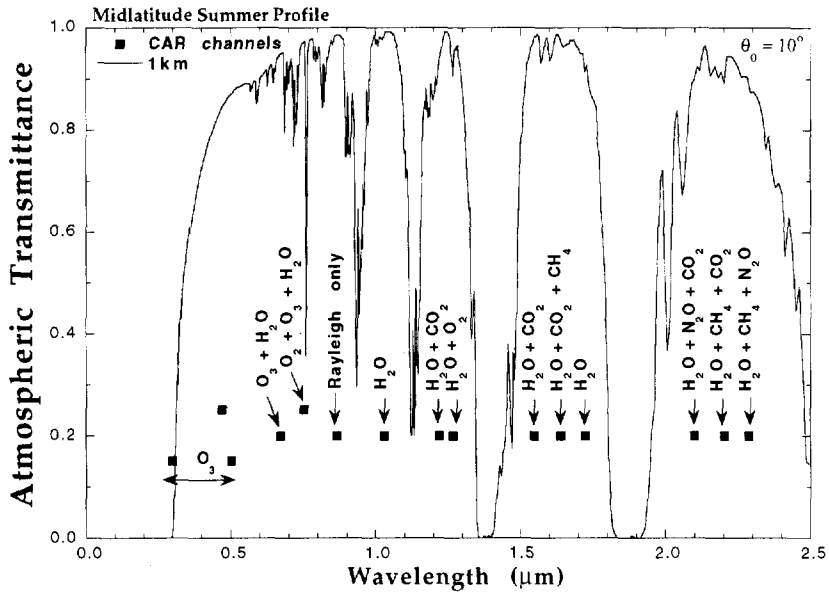

Figure 1. Clear-sky transmittance and the relative positions of cloud absorption radiometer (CAR) channels (see text for details).

3. Instrumentation and Data Collection

During SCAR-B, measurements of surface bidirectional reflectance were acquired by using a multispectral, scanning radiometer, the cloud absorption radiometer (CAR), which was designed and built at the NASA Goddard Space Flight Center [cf. *King et al.*, 1986, for details]. In brief the CAR, mounted in the nose of the University of Washington C-131A research aircraft, provides radiometric measurements at 13 discrete wavelengths between 0.3 and 2.3 μm. Figure 1 shows the clear-sky atmospheric transmittance and relative positions of the CAR channels. A midlatitude summer atmosphere [*Anderson et al.*, 1986] was used to compute the transmittance from the top of the atmosphere to 1 km height. As shown in Figure 1, all of the CAR channels were carefully selected to minimize the effects of gaseous absorption, except for the UV-B channel where ozone absorption is desired. They are centered at wavelengths of 0.307 (or 0.754, interchangeable but not used in SCAR-B), 0.472 (or 0.507), 0.675, 0.869, 1.038, 1.219, 1.271, 1.552, 1.643, 1.725, 2.099, 2.207, and 2.303 μm. The CAR channels at the visible wavelengths are affected weakly by ozone absorption (i.e., Chappuis band) and more by Rayleigh scattering, resulting in a total of about 3–12% reduction in atmospheric transmittance. However, both of these effects are well known and relatively easy to correct. The 0.869 and 1.038 μm bands are the cleanest window channels, where both Rayleigh scattering and ozone absorption are largely negligible. In the shortwave-infrared channels, water vapor and trace gas absorption can produce about 2–8% reduction in atmospheric transmittance.

The optical system of the CAR is nondispersive, being composed of a complex configuration of dichroic beam splitters and narrowband interference filters. The filter wheel contains optical channels 8–13 (i.e., 1.552–2.303 μm) and can be locked at a particular channel or rotated to measure a new wavelength interval after a preset number of scans. In general, the bandwidth of the CAR channels is about 20 nm, except for the filter wheel channels where $\Delta\lambda \approx 40$ nm. With this configuration the first seven channels are continuously and simultaneously sampled, while the eighth registered channel is selected from among the six channels on the filter wheel. To allow for the large variations in absolute magnitude of the radiance arising as a function of optical properties of the target and especially the solar zenith angle, the CAR provides for seven manual gain selections that apply a uniform gain adjustment to all eight electrical channels simultaneously. This manual gain setting, which permits greater flexibility in field operations, is output to the data system for retrieval.

Viewing with an IFOV of 1°, the CAR scans in a vertical plane on the right-hand side of the aircraft from 5° before zenith to 5° past nadir (190° aperture), thereby permitting observations of both the zenith and the nadir radiances to be obtained with as much as a 5° aircraft roll, an angle measured simultaneously with a gyroscope aboard the aircraft. In addition, by rotating the instrument 90° around the aircraft's principal axis, the CAR can also be used as a downward looking, cross-track imager. This imaging capability was successfully demonstrated during SCAR-B. Table 1 summarizes the CAR specifications.

By definition (equation (2)) the BRF describes the angular distribution of reflected radiances from an element of surface

Table 1. Cloud Absorption Radiometer Specifications During SCAR-B

	Specifications
Platform	University of Washington C-131A aircraft
Ground speed	80 m s^{-1} (nominal)
Total field of view	190°
Instantaneous field of view	17.5 mrad (1°)
Pixels per scan line	395
Scan rate	100 scan lines per minute
Spectral channels	13 (7 continuously sampled and 6 in filter wheel)
Spectral range	0.307–2.303 μm
Data system	eight channels @ 10 bits
Calibration	integrating sphere on the ground

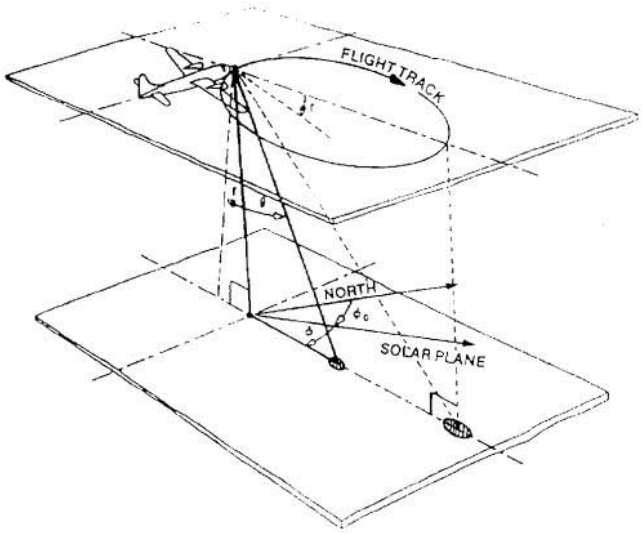

Figure 2. Schematic illustration of a clockwise circular flight track for measuring both the reflected and the transmitted solar radiation.

area, in terms of which the setup of instrumentation should resemble a sensor with a goniometer [cf. *Perovich*, 1994, Figure 1] looking at a particular area with all selected viewing angles. Although the goniometer approach, as frequently adopted by geologists, provides a more precise bidirectional geometry, it suffers from sampling inefficiency for most remote sensing applications. With such deployment, the spatial resolution is generally far less than 1 m due to the size limitation of the goniometer, and the measurements are susceptible to the fine variation of specific properties of the targeted surface area. Hence a large volume of samples obtained under identical source and surface conditions is required. For airborne measurements the goniometer-like sampling strategy is even more difficult to implement, mainly due to the requirement of a long observation period. Alternatively, if the average conditions of the targeted surface area are nearly homogeneous, the approach depicted in Figure 2 should provide the most mobile and efficient means for airborne measurements of surface bidirectional reflectance.

In Figure 2 the operational specifications for the CAR in measuring the surface bidirectional reflectance are shown. The average speed of the C-131A is about 80 m s^{-1}, which results in a minimum circle of about 3 km in diameter at a comfortable roll angle of 20° in about 2 min. At an altitude of 600 m above the targeted surface area and 1° IFOV, the pixel resolution is about 10 m at nadir and about 270 m at an 80° viewing angle from the CAR. During the SCAR-B campaign, four types of surface bidirectional reflectances were obtained under this flight track: cerrado, dense forest, dense smoke layer, and reservoir water.

Figure 3 shows an example of CAR measurements in a time series of spectral (e.g., 1.271 μm) imagery for flight 1701 (1321–1358 UT, September 6, 1995) near Porto Velho, Brazil. The top half of the image strip (0°–90°, 0° for zenith) denotes the measurements of sky radiance and the bottom half (90°–180°, 180° for nadir) surface-reflected radiances. As demonstrated by the 1.271 μm channel, the vegetated surface appears bright, and the effect of aerosol scattering is reduced. At the beginning of the image the CAR was scanning in the principal plane, where the solar disk (bright spot in the top part) and the corresponding specular reflection from the river water are clearly seen. Since the image was not presented in a proper aspect ratio, the solar disk appears as an oval shape. The black rectangular boxes around the nadir-viewing direction were the missing data due to sharp turning of aircraft (banking to the left with roll angle >5°). The bottom half of the last 12-min of the image demonstrates the measurements of surface bidirectional reflectance, as depicted in Figure 2. Replicated observations (multiple circular orbits) were acquired for every selected surface.

4. Results From Observations

The fundamental assumption involved in reconstructing a bidirectional reflectance from CAR measurements is the homogeneity of the targeted surface area. By selecting the targets carefully, the approach depicted in Figure 2 should prove the most mobile and efficient means of measuring surface bidirectional reflectance. During SCAR-B the spectral BRF measurements for four types of surfaces were selected and obtained in five CAR flight missions. They are as follows: (1) cerrado, acquired in Goias, north of Brasília, under nearly clear-sky conditions, from 1851 to 1902 UTC on August 18, 1995 (flight 1689); (2) dense forest, acquired northwest of Cuiabá, Mato Grosso, under nearly clear-sky conditions, from 1905 to 1911 UTC and from 1917 to 1923 UTC on August 25, 1995 (flight 1693); (3) thick smoke layer over dense forest, acquired northeast of Porto Velho, Rondonia, with nearly clear sky above, from 1342 to 1355 UTC on September 6, 1995 (flight 1701), with similar data also acquired on September 11, 1995 (flight 1704); and (4) reservoir water with tree debris, acquired southeast of Porto Velho, Rondonia, under broken cloud conditions, from 1817 to 1826 UTC on September 7, 1995 (flight 1703).

Plates 1a, 1b, and 1c show photographs of cerrado, dense forest, and heavy smoke, taken from the University of Washington C-131A aircraft around the time the spectral measurements of surface bidirectional reflectance were obtained. Since the CAR data of reservoir water were acquired under broken

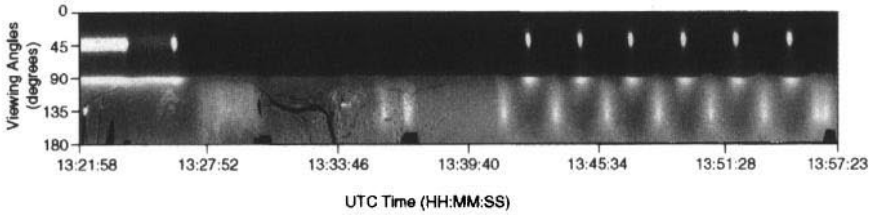

Figure 3. Example of CAR measurements (1.271 μm) in a time series (1321–1358 UT) on September 6, 1995, during SCAR-B (see text for details).

Table 2. Computed Spectral Albedo and Measured Nadir Reflectance for Cerrado, Dense Forest, and Thick Smoke Layer Over Forest

Central Wavelength, μm	Bandwidth, μm	Solar flux, $Wm^{-2}\mu m^{-1}$	Solar Zenith Angle	Albedo	Nadir Reflectance
		Cerrado, August 18, 1995			
0.472	0.021	1974.4	59.07°–61.73°	0.061 ± 0.0021	0.036 ± 0.0063
0.675	0.020	1480.4	59.07°–61.73°	0.081 ± 0.0027	0.062 ± 0.0194
0.869	0.020	949.13	59.07°–61.73°	0.260 ± 0.0026	0.203 ± 0.0347
1.038	0.020	675.07	59.07°–61.73°	0.305 ± 0.0035	0.241 ± 0.0390
1.219	0.020	477.86	59.07°–61.73°	0.284 ± 0.0043	0.239 ± 0.0341
1.271	0.021	433.33	59.07°–61.73°	0.311 ± 0.0049	0.264 ± 0.0375
1.643	0.041	230.99	59.63°–60.71°	0.280	0.239 ± 0.0449
2.207	0.040	72.672	61.22°–61.73°	0.174	0.153 ± 0.0314
		Dense Forest, August 25, 1995			
0.472	0.021	1979.4	54.79°–58.56°	0.039 ± 0.0062	0.015 ± 0.0043
0.675	0.020	1484.1	54.79°–58.56°	0.030 ± 0.0031	0.013 ± 0.0126
0.869	0.020	951.55	54.79°–58.56°	0.284 ± 0.0177	0.233 ± 0.0357
1.038	0.020	676.79	54.79°–58.56°	0.325 ± 0.0087	0.267 ± 0.0331
1.219	0.020	479.07	54.79°–58.56°	0.268 ± 0.0055	0.225 ± 0.0288
1.271	0.021	434.43	54.79°–58.56°	0.289 ± 0.0061	0.246 ± 0.0317
1.643	0.041	231.57	54.79°–55.87°	0.198	0.170 ± 0.0607
2.207	0.040	72.857	56.96°–58.56°	0.071	0.055 ± 0.0246
		Smoke Layer, September 6, 1995			
0.472	0.021	1989.8	39.14°–36.36°	0.174 ± 0.0020	0.105 ± 0.0019
0.675	0.020	1491.9	39.14°–36.36°	0.114 ± 0.0015	0.059 ± 0.0036
0.869	0.020	956.55	39.14°–36.36°	0.308 ± 0.0014	0.284 ± 0.0105
1.038	0.020	680.34	39.14°–36.36°	0.327 ± 0.0021	0.314 ± 0.0132
1.219	0.020	481.59	39.14°–36.36°	0.223 ± 0.0020	0.220 ± 0.0093
1.271	0.021	436.72	39.14°–36.36°	0.276 ± 0.0030	0.271 ± 0.0121
1.643	0.041	232.79	39.14°–38.05°	0.155	0.144 ± 0.0095
2.207	0.040	73.240	37.49°–36.36°	0.063	0.059 ± 0.0099

cloud conditions, the solar disk was not clearly visible, and the distribution of diffuse sky radiance was very complex. Understanding that data set better requires thorough radiative transfer modeling and is beyond the scope of this paper. In addition, the 0.307 μm channel was designed specifically for studying ozone UV-B absorption and will not be presented here. Below, we will document and discuss the results of BRF measurements obtained from the CAR on three types of surfaces.

4.1. Cerrado on August 18, 1995

As shown in the photograph of Plate 1a, cerrado (savannah) is mainly composed of scrub-like vegetation, in which the ground cover is uniform but not very dense. Five circular orbits were made to produce replicated BRF observations in order to average out surface inhomogeneity. For the first three orbits the filter wheel channel was locked at the 1.643 μm band, and the last two orbits at the 2.207 μm band. Within this observational period (~11 min) the solar zenith angle varied from 59.07° to 61.73° (compare Table 2). Since fewer data were taken for the filter wheel channels, their variations in solar zenith angle were smaller. The background aerosol loadings were reported to be very low by the C-131A meteorologist, and the retrieved aerosol optical thickness at 0.67 μm channel from the Sun photometer was less than 0.1 in the vicinity of Brasília.

Plate 2 demonstrates the spectral BRF measured over cerrado. In all polar plots, zenith is represented as radial distance from the center, azimuth as length of the arc on the respective zenith circle. The principal plane resides in the 0°–180° azimuthal plane with the Sun located in the 180° azimuth direction. With this definition the top half circle represents forward scattering and the lower half for backscattering, with the antisolar direction at $\theta_0 \approx 60°$, shown as a white spot in Plate 2a.

Two striking features appear clearly in Plate 2: a highly symmetric pattern and a strong reflection in the backscattering direction. Although the averaged BRF data from all circles have further smoothed and symmetrized the bidirectional reflectance pattern, yielding good statistics in representing cerrado, BRF data from an individual circle are not much different from one another. The observed strong backscattering signal, peaked at ~60° zenith angle in the principal plane at $\phi = 180°$, is known as the "hot spot" or "opposition surge" [*Hapke*, 1993]. For this case, the reflection functions have values near or close to 0.6 in the 0.869–1.643 μm region. Apparently, the spectral and angular information, such as the amplitude and width of the hot spot feature, are closely related to the specific biophysical parameters (e.g., leaf size, shape, density). The surface spectral anisotropy retains similar patterns but becomes less pronounced in the visible region due to chlorophyll absorption as well as strong light scattering by the atmosphere. This is clearly seen in the blue channel (0.472 μm), in which the range of backscattering peak is broadened.

To investigate the detailed angular distribution of BRF, Plate 3 shows the spectral dependence of the reflection function along the principal plane. The amplitude and angular width of the hot spot for cerrado (Plate 3a), located at ~60° (a few degrees off at 2.207 μm due to time differences), reveals strong spectral dependence. In the 0.869–1.271 μm range, the shape of the hot spot is spiky; while its amplitude is reduced and becomes broader toward longer (e.g., 2.207 μm) or shorter (e.g., 0.675 μm) wavelengths. A secondary peak of backscat-

tering exists near $\theta \approx 75°$ for the 0.869–1.271 μm channels and is greatly suppressed at the 0.675, 1.643, and 2.207 μm channels. This phenomenon may be related to the multiple scattering among leaves with particular leaf angle distributions [e.g., *Ross and Marshak*, 1989]. Reflection functions for all channels show limb darkening in the backscattering horizon direction, except for the blue (0.472 μm) channel where Rayleigh scattering becomes dominant. In the forward scattering portion, limb brightening is clearly seen at the horizon for all channels. Whether these limb darkening and brightening features are solely (or in part) due to atmospheric effect or surface BRF itself remain to be explored through modeling.

4.2. Dense Forest on August 25, 1995

Starting from August 23, 1995, the University of Washington C-131A aircraft was based at Cuiabá, north of the Pantanal, the largest wetlands in the world. As shown in the photograph of Plate 1b, the area of dense forest is covered by tall trees with a large canopy, in which the ground surface is invisible. On August 25, 1995, the BRF data with the 1.643 μm channel were first acquired over the dense forest, and then corrected for aircraft drift due to cross wind. Another set of BRF data with the 2.207 μm channel were obtained over the same site. Within the two observational periods (~18 min) the solar zenith angle varied from 54.79° to 58.56° (compare Table 2). Since fewer data were taken for both filter wheel channels, their variations in solar zenith angle were small. In addition, at the time these BRF measurements were obtained, the background aerosol loading was reported to be relatively low by the C-131A meteorologist. However, the retrieved aerosol optical thickness at the 0.67 μm channel from the Sun photometer reached about 0.24 in the vicinity of Cuiabá on this day.

Plate 4 shows the spectral BRF over dense forest which we obtained on this day. As was the case over cerrado (compare Plate 2), these data reveal a good symmetric pattern, suggesting a rather homogeneous surface. However, the details of the spectral BRF (e.g., the strength and angular width of the hot spot) are quite different for the dense forest as compared to the cerrado, due largely to the different type and coverage of green biomass. In the visible (e.g., 0.472 and 0.675 μm) and shortwave-infrared (e.g., 1.643 and 2.207 μm) regions the BRF values over dense forest were generally about half of that over cerrado, as shown in Plate 3b of the principal plane plot. (Note that the BRF plot of 2.207 μm in Plate 4 was doubled for the purpose of showing better contrast.) This can be explained by the difference of spectral characteristics between soil and green biomass. In the 0.869–1.271 μm region the spectral reflectance of both soil and green biomass is bright, and the magnitude of the BRF for dense forest and cerrado are comparable but different in shape, especially for the hot spot and the secondary plateau (~75°, depicted in Plate 3b) in the backscattering direction. Complete radiative transfer modeling is required to fully understand these photon-vegetation interactions.

4.3. Smoke Layer Over Dense Forest on September 6, 1995

Beginning on September 5, 1995, the University of Washington C-131A aircraft was based at Porto Velho, near the edge of the world's largest tropical rain forest, the Amazon. As shown in the photograph of Plate 1, the smoke layer is optically thick and resembles a modeled plane-parallel atmosphere in which the ground surface is invisible in the visible wavelengths. On September 6, 1995, the BRF data with the 1.643 and 2.207 μm channels were acquired above the smoke layer overlying dense forest about 100 miles northeast of Porto Velho. Within this observational period (~13 min) the Sun was high and the solar zenith angles decreased from 39.14° to 36.36° (compare Table 2). Since fewer data were taken for both filter wheel channels, their variations in solar zenith angle were relatively small. As reported by the C-131A meteorologist, the top of the smoke layer reached about 4000 m at the time these BRF measurements were obtained, with a cloud cover that was much less than 1%. In addition, the retrieved aerosol optical thickness at 0.67 μm from nearby Sun photometer sites generally exceeded 1.5 when the sky was cloud free.

In Plate 5 the BRFs at 1.643 and 2.207 μm were doubled to show better contrast. All BRF measurements obtained for the thick smoke layer over dense forest reveal fairly smooth and symmetric patterns, due to the homogeneous coverage of the forest surface and the enhancement from aerosol multiple scattering (also see Plate 3c). In the visible (e.g., 0.472 and 0.675 μm), aerosol scattering effects dominate, and the hot spot feature from the underlying vegetated surface is diminished due to enhancement from aerosol multiple scattering. This is also the main reason that the broad plateau in the backscattering direction for the 0.869–1.271 μm range is completely suppressed. In the shortwave-infrared (e.g., 1.643 and 2.207 μm) regions the hot spot can be clearly seen and little affected by aerosol scattering. As suggested by *Kaufman and Tanré* [1996], an alternative way to locate dark pixels in remote sensing applications is to use shortwave-infrared channels (e.g., 2.207 μm), because they are less affected by aerosols but are still sensitive to surface characteristics. Thus in the visible channels (e.g., blue, green, and red) the surface albedo of dark pixels underlying a heavy aerosol layer can be inferred, provided a spectral correlation of BRF between 2.207 μm and a visible channel exists.

4.4. Spectral Albedo

The spectral BRF measurements by the CAR contain very fine angular resolution (i.e., $M = 90$ samples in θ and $N \approx 200$ in ϕ; compare Table 1) which produces virtually no computational error in discretizing the integral. By using (3) it is straightforward to compute the spectral-hemispherical albedo for the cerrado, dense forest, and heavy smoke over dense forest. Table 2 lists the central wavelength and bandwidth characteristics of each CAR channel, together with the corresponding solar flux computed by weighting the solar flux at the top of the atmosphere with the spectral response function of each band. The solar fluxes vary slightly from day to day due to the elliptical orbit of the Earth about the Sun. In column 4 the variation of solar zenith angle is shown for the period of data collection. Since the change of solar zenith angle is quite small over the time period of the measurements, generally in the range of 1°–3°, this results in only a small variation in the computed spectral albedo (column 5) due largely to surface inhomogeneity. Generally, the spectral albedo between the cerrado and the dense forest differs by less than about 0.05 (within a few degrees difference in solar zenith angles) but with different shapes spectrally. When the smoke layer is present, the dark forest becomes brighter (even for smaller zenith angle) in the visible wavelengths, due to the enhancement of aerosol multiple scattering. In column 6 of Table 2, the statistics of nadir reflectances are listed. Comparing the computed albedo to the measured nadir reflectance, often used as a surrogate for surface in climate models, the error is typically

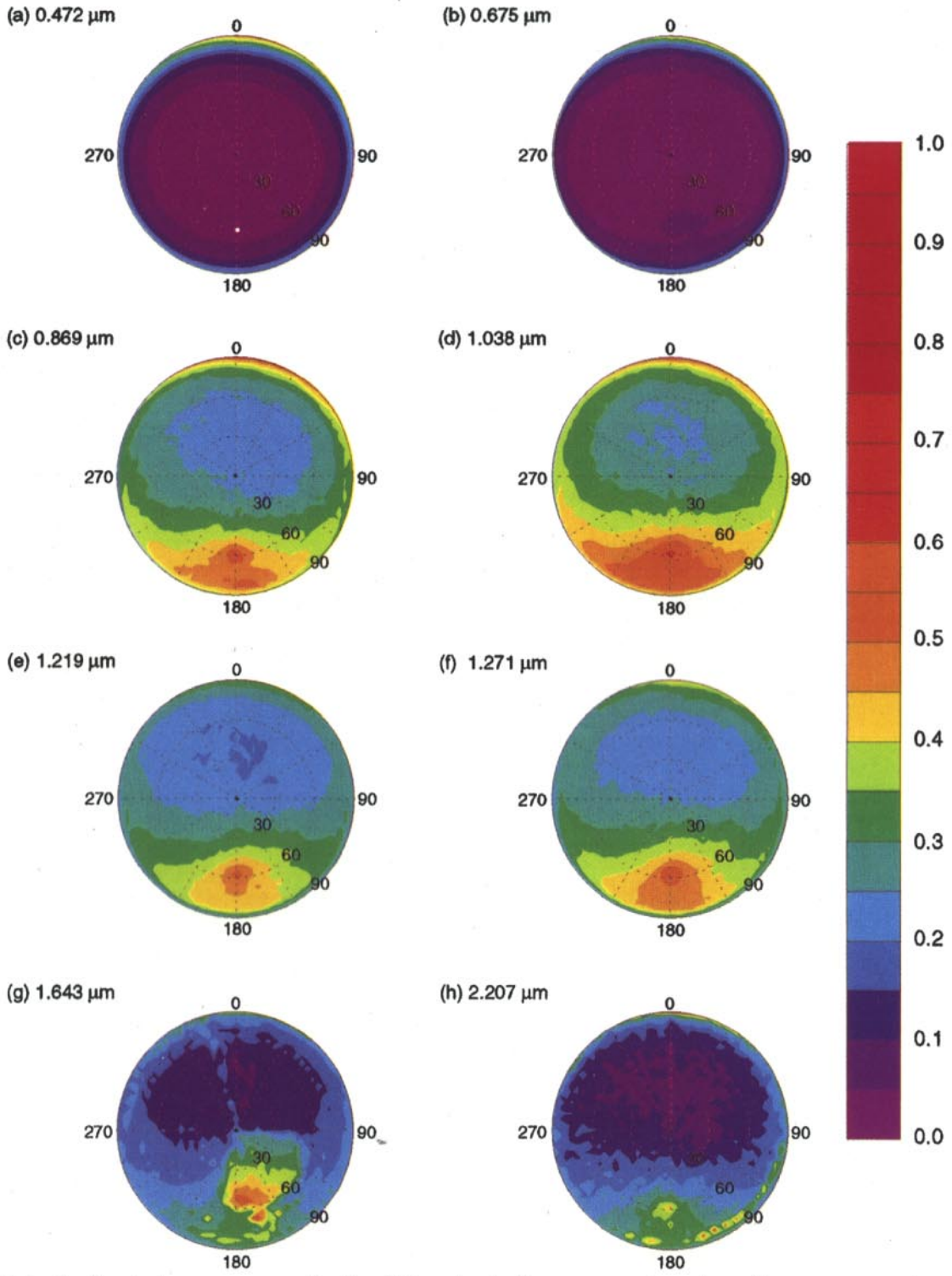

Plate 4. Spectral measurements of surface bidirectional reflectance over dense forest (large canopy type) on August 25, 1995, during SCAR-B. Note that the BRF of 2.207 μm was doubled to show better contrast.

about 10–20%, with some extremes of up to 60%, depending on solar zenith angle. Thus from the CAR measurements during SCAR-B the estimation of spectral-hemispherical albedo from nadir reflectance produces large underestimates of the true albedo.

5. Summary

In the upcoming EOS era, satellite remote sensing will play a major role in the interpretation of the Earth climate system at large space and timescales and is expected to provide com-

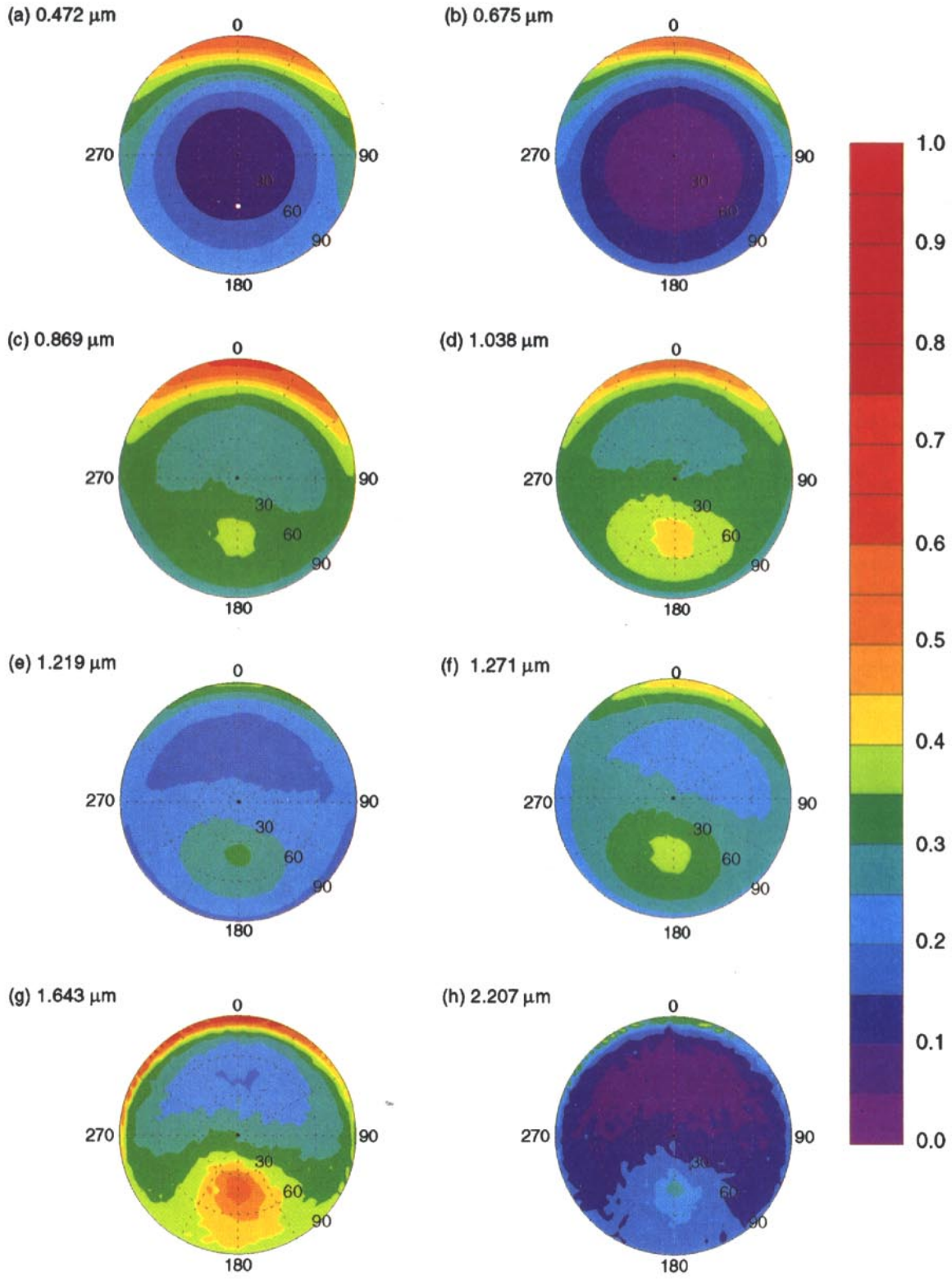

Plate 5. Spectral measurements of surface bidirectional reflectance above smoke layer (over dense forest) on September 6, 1995, during SCAR-B. Note that the BRFs of 1.643 and 2.207 μm were doubled to show better contrast.

prehensive statistics for GCM input and validation and for monitoring climate changes. Radiances obtained from satellite measurements pertain to the surface-atmosphere system as a whole, whereas bidirectional reflectance is an intrinsic property of the surface under specified illumination conditions [e.g., *Wanner et al.*, 1997]. An accurate description of surface anisotropy is essential for reliable prediction and proper interpretation of satellite measurements. Detailed measurements of the spectral bidirectional reflectance properties of natural surfaces are crucial to understanding and modeling their physical and

radiative properties, as well as for aiding in the remote sensing of aerosols and clouds above natural surfaces. One such opportunity to measure surface anisotropy was enabled using an aircraft scanning radiometer during the SCAR-B field campaign.

During SCAR-B, surface spectral bidirectional reflectance patterns of cerrado (August 18, 1995), dense forest (August 25, 1995), and thick smoke layers over dense forest (September 6 and 11, 1995) were measured using the cloud absorption radiometer (CAR) under nearly clear-sky conditions. All BRF data were processed to level 1b (calibrated and geolocated radiances). In addition, browse images, a CAR data user's guide, software for unpacking and interpreting the data, and information on where and how to obtain data are accessible via World Wide Web (http://climate.gsfc.nasa.gov/CAR).

Although the CAR measurements are contaminated by minor atmospheric effects, results show distinct spectral characteristics for three types of surfaces. The spectral BRF of cerrado, dense forest, and heavy smoke over dense forest revealed fairly symmetric patterns around the principal plane, with varying amplitudes and angular widths of the hot spot (backscattering peak in the antisolar direction). In the shortwave-infrared region the aerosol effect is very small due to low spectral optical depth, and these hot spots are clearly seen in the bidirectional reflectance of the smoke layer over dense forest. In the 0.869–1.271 μm range the hot spot has a spiky shape, but it reduces in strength and becomes broader toward longer (e.g., 1.643 and 2.207 μm) and shorter (e.g., 0.472 and 0.675 μm) wavelengths, where, respectively, the leaf water and chlorophyll absorption prevails. A broad plateau in the backscattering direction exists near $\theta = 75°$ for the 0.869–1.271 μm range, observed over the cerrado and dense forest (but not for the smoke layer) and diminished for the 0.675, 1.643, and 2.207 μm channels. This phenomenon may be related to multiple scattering among leaves with particular leaf angle distributions [e.g., *Ross and Marshak*, 1989].

These detailed measurements of the angular distribution of spectral reflectance have been used to compute surface albedo. Large differences are found between these spectral-hemispherical albedos and those of the measured nadir reflectance. These angular and spectral dependencies can be utilized to retrieve either surface characteristics, using a few independent parameters, or aerosol microphysical and optical properties (e.g., size distribution and single-scattering parameters), if proper physical and radiation models are used. The CAR measurements, combined with the boundary layer aircraft measurements of aerosol physical properties and radiosonde observations, form an unprecedented data set with many scientific results anticipated following more extensive radiative transfer modeling in the future.

Acknowledgments. The authors are especially grateful to P. V. Hobbs and all of the University of Washington personnel for helping to make this complex field project and data collection a success. This research was supported by funding provided by the MODIS Science Team, the EOS Project Science Office, and NASA's Radiation Science Program.

References

Anderson, G. P., S. A. Clough, F. X. Kneizys, J. H. Chetwynd, and E. P. Shettle, AFGL atmospheric constituent profiles (0–120 km), *AFGL-TR-86-0110*, Air Force Geophys. Lab., Bedford, Mass., 1986.

Asrar, G., and R. Greenstone (Eds.), 1995 MTPE/EOS reference handbook, *NASA Rep. NP-215*, 277 pp., 1995.

Barnsley, M. J., Effect of off-nadir view angles on the detected spectral response of vegetation canopies, *Int. J. Remote Sens.*, *5*, 715–728, 1984.

Barnsley, M. J., A. H. Strahler, K. P. Morris, and J.-P. Muller, Sampling the surface bidirectional reflectance distribution function (BRDF), 1, Evaluation of current and future satellite sensors, *Remote Sens. Rev.*, *8*, 271–311, 1994.

Deering, D. W., E. M. Middleton, J. R. Irons, B. L. Blad, E. A. Walter-Shea, C. J. Hays, C. Walthall, T. F. Eck, S. P. Ahmad, and B. P. Banerjee, Prairie grassland bidirectional reflectances measured by different instruments at the FIFE site, *J. Geophys. Res.*, *97*, 18,887–18,903, 1992.

Hapke, B., *Theory of Reflectance and Emittance Spectroscopy*, 455 pp., Cambridge Univ. Press, New York, 1993.

Kaufman, Y. J., and D. Tanré, Strategy for direct and indirect methods for correcting the aerosol effect on remote sensing: From AVHRR to EOS-MODIS, *Remote Sens. Environ.*, *55*, 65–79, 1996.

Kaufman, Y. J., et al., The Smoke, Clouds, and Radiation experiment in Brazil (SCAR–B), *J. Geophys. Res.*, this issue.

Kimes, D. S., and P. J. Sellers, Inferring hemispherical reflectance of the earth's surface for global energy budgets from remotely-sensed nadir or directional radiance values, *Remote Sens. Environ.*, *18*, 205–223, 1985.

Kimes, D. S., P. J. Sellers, and D. J. Diner, Extraction of spectral hemispherical reflectance (albedo) of surface from nadir and directional reflectance data, *Int. J. Remote Sens.*, *8*, 1727–1746, 1987.

King, M. D., Directional and spectral reflectance of the Kuwait oil-fire smoke, *J. Geophys. Res.*, *97*, 14,545–14,549, 1992.

King, M. D., M. G. Strange, P. Leone, and L. R. Blaine, Multiwavelength scanning radiometer for airborne measurements of scattered radiation within clouds, *J. Atmos. Oceanic Technol.*, *3*, 513–522, 1986.

Kriebel, K. T., Measured spectral bidirectional reflectance properties of four vegetated surfaces, *Appl. Opt.*, *17*, 253–259, 1978.

Kriebel, K. T., Albedo of vegetated surface: Its variability with different irradiances, *Remote Sens. Environ.*, *8*, 283–290, 1979.

Nicodemus, F. E., J. C. Richmond, J. J. Hsia, I. W. Ginsberg, and T. Limperis, Geometrical considerations and nomenclature for reflectance, *NBS Monogr.*, *160*, 1–52, 1977.

Perovich, D. K., Light reflection from sea ice during the onset of melt, *J. Geophys. Res.*, *99*, 3351–3359, 1994.

Pinty, B., and M. M. Verstraete, Extracting information on surface properties from bidirectional reflectance measurements, *J. Geophys. Res.*, *96*, 2865–2874, 1991.

Ranson, K. J., J. R. Irons, and C. S. T. Daughtry, Surface albedo from bidirectional reflectance, *Remote Sens. Environ.*, *35*, 201–211, 1991.

Ranson, K. J., J. R. Irons, and D. L. Williams, Multispectral bidirectional reflectance of northern forest canopies with Advanced Solid-State Array Spectroradiometer (ASAS), *Remote Sens. Environ.*, *47*, 276–289, 1994.

Ross, J. K., and A. L. Marshak, The influence of leaf orientation and the specular component of leaf reflectance on the canopy bidirectional, *Remote Sens. Environ.*, *27*, 251–260, 1989.

Salomonson, V. V., and W. E. Marlatt, Anisotropic solar reflectance over white sand, snow, and stratus clouds, *J. Appl. Meteorol.*, *7*, 475–483, 1968.

Strahler, A. H., and D. L. B. Jupp, Modeling bidirectional reflectance of forest and woodlands using Boolean models and geometric optics, *Remote Sens. Environ.*, *34*, 153–166, 1990.

Suits, G. H., The calculation of the directional reflectance of a vegetation canopy, *Remote Sens. Environ.*, *2*, 117–125, 1 972.

van de Hulst, H. C., *Multiple Light Scattering: Tables, Formulas, and Applications*, 739 pp., Academic, San Diego, Calif., 1980.

Wanner, W., A. H. Strahler, B., Hu, P. Lewis, J. P. Muller, X. Li, C. L. Barker Schaaf, and M. J. Barnsley, Global retrieval of bidirectional reflectance and albedo over land from EOS MODIS and MISR data: Theory and algorithm, *J. Geophys. Res.*, *102*, 17,143–17,161, 1997.

G. T. Arnold and J. Y. Li, Space Applications Corporation, 901 Follin Lane, Suite 400, Vienna, VA.

M. D. King and S.-C. Tsay, NASA Goddard Space Flight Center, Code 913, Greenbelt, MD 20771. (e-mail: tsay@climate.gsfc.nasa.gov)

(Received October 6, 1997; revised April 2, 1998;
accepted April 2, 1998.)